Geophysical Research Letters

RESEARCH LETTER
10.1029/2025GL119535

Hiss Wave Evolution During Substorms Based on Van Allen Probes Observations

Xiao-Chen Shen[1], Wen Li[1], Qianli Ma[1,2], Nigel P. Meredith[3], Xiangning Chu[4], Murong Qin[1], Luisa Capannolo[1], and Sheng Huang[1]

[1]Center for Space Physics, Boston University, Boston, MA, USA, [2]Department of Atmospheric and Oceanic Sciences, University of California, Los Angeles, CA, USA, [3]British Antarctic Survey, Natural Environment Research Council, Cambridge, England, [4]Laboratory for Atmospheric and Space Physics, University of Colorado Boulder, Boulder, CO, USA

Abstract Hiss waves frequently occur in the plasmasphere or plumes, playing a key role in energetic electron loss in the Earth's inner magnetosphere. While previous studies have linked hiss wave enhancements in the outer plasmasphere (just inside the plasmapause) to electron injections during substorms, their evolution across various substorm phases remains unclear. Using Van Allen Probes observations over 2013–2019, we evaluate hiss wave evolution during various phases of substorm activity. At $L > 4$, both hiss wave intensity and energetic electron flux increase shortly after substorm onset, first on the morning side, then progress to later magnetic local times (MLTs) at a rate of ∼1–3 hr MLT per hr in universal time (UT), eventually stabilizing near 13 MLT. Stronger substorms result in larger and faster intensification in hiss wave intensity and have more significant impact at lower L-shells. Our results highlight the global variation of hiss waves during substorms.

Plain Language Summary Hiss waves are one of the most important plasma waves in Earth's plasmasphere. They can scatter electrons trapped in the magnetosphere, causing them to fall into the atmosphere and contributing to form the slot region between the inner and outer radiation belts. While it is known that hiss wave activity is influenced by substorms, their evolution over time and across different regions of the magnetosphere is not fully understood. In this study, we use high-quality wave measurements from the dual Van Allen Probes, which provided extensive coverage over the entire mission period, to examine the global hiss wave evolution during substorms. We found that hiss waves intensify immediately after substorm onset on the morning side and then progress to later magnetic local times (MLTs), eventually stabilizing around 13 MLT. Energetic electrons at 60 keV show a similar pattern to hiss waves. Moreover, stronger substorms lead to larger and faster wave intensification and affect lower L-shells more significantly. These findings improve our understanding of hiss wave evolution on a global scale during substorms.

Key Points:

- Global evolution of hiss waves during 4,071 substorm events is evaluated using Van Allen Probes data
- Hiss wave amplitude and energetic electron fluxes intensify nearly simultaneously following substorm onset
- Hiss wave activity progresses from ∼6 magnetic local time (MLT) toward later MLTs at ∼1–3 MLT hr/UT hr, stabilizing near ∼13 MLT

Supporting Information:

Supporting Information may be found in the online version of this article.

Correspondence to:

X.-C. Shen,
sdusxc@gmail.com

Citation:

Shen, X.-C., Li, W., Ma, Q., Meredith, N. P., Chu, X., Qin, M., et al. (2026). Hiss wave evolution during substorms based on Van Allen Probes observations. *Geophysical Research Letters*, *53*, e2025GL119535. https://doi.org/10.1029/2025GL119535

Received 17 SEP 2025
Accepted 18 FEB 2026

1. Introduction

Hiss waves are right-hand polarized electromagnetic waves commonly observed in Earth's high-density plasmasphere and plasmaspheric plume regions, typically spanning frequencies from tens of Hz to several kHz (He et al., 2019, 2020; Li et al., 2013; Thorne et al., 1973). Their distribution presents a pronounced day-night asymmetry, with stronger hiss wave power observed on the dayside (Chu et al., 2024; Meredith et al., 2018; Spasojevic et al., 2015). Hiss waves may be generated through several mechanisms: local amplification by energetic electrons (He et al., 2019, 2020; Meredith et al., 2006; Tsurutani et al., 2018), propagation from chorus waves (Bortnik et al., 2008, 2009; Li et al., 2015; Meredith et al., 2013, 2021), or propagation from lightning-generated whistlers (Draganov et al., 1992; Hayakawa & Sazhin, 1992; Meredith et al., 2006; Sonwalkar & Inan, 1988; Thorne et al., 1973).

Hiss waves play a crucial role in shaping the radiation belts, which are key components of space weather. Through wave-particle interactions, hiss waves can scatter electrons with energies ranging from several keV to hundreds of keV into the bounce loss cone (Li et al., 2019; Ma et al., 2021; Shen et al., 2023), leading to their precipitation into the atmosphere (Li et al., 2014; Millan & Thorne, 2007; Ni et al., 2013). These waves are also critical for forming the slot region between the inner and outer radiation belts (Kim et al., 2020; Meredith et al., 2007), and contribute to the development of inverted energy spectra, known as "bump-on-tail" distribution (Ma et al., 2016; Zhao et al., 2019). In addition, case studies suggest that hiss waves may drive modulated energetic electron precipitation, influenced by modulating solar wind structures (Breneman et al., 2015).

Extensive studies have shown that hiss wave activity is highly dependent on geomagnetic conditions. During quiet periods, plasmaspheric hiss waves are suggested to be generated through the propagation from chorus waves outside the plasmasphere into the plasmasphere (Bortnik, Chen, Li, Thorne, & Horne, 2011; Bortnik, Chen, Li, Thorne, Meredith, & Horne, 2011; Bortnik et al., 2008). Following substorm onset, injected electrons and the reconfigured plasmasphere/plume structure create conditions that support local hiss amplification and, in certain regions (e.g., dayside and plume sectors), can also enable contributions from chorus-to-hiss propagation (Bortnik et al., 2008; Liu et al., 2020; Meredith et al., 2013, 2021). Statistical studies have shown that hiss wave power increases during substorms with wave activity extending to higher L-shells (Meredith et al., 2004). A possible reason is the efficient chorus-to-hiss conversion during active times, as further supported by observed correlations between chorus and hiss during substorms (Chen et al., 2012; Meredith et al., 2004). During the recovery phase, plasmaspheric hiss persists, preferentially on the dayside, and continues to drive energetic electron losses in the outer radiation belt (Agapitov et al., 2020; Ma et al., 2016; Meredith et al., 2018; Zhang et al., 2019).

However, the global temporal evolution of hiss waves throughout various phases of substorms remains elusive, especially the magnetic local time (MLT) progression of the hiss enhancement region and their dependence on substorm activities. In this study, we leverage high-quality wave measurements provided by the dual Van Allen Probes to assess these features and quantify the global temporal evolution of hiss waves during substorms.

2. Data Set and Methodology

We use plasma wave and energetic electron measurements from the Van Allen Probes (RBSP) mission (Mauk et al., 2013). The two probes, with an apogee around 5.8 R_E, are ideal for measuring hiss waves in plasmasphere or plumes. Hiss waves are measured by the Waveform Receiver from the Electric and Magnetic Field Instrument Suite and Integrated Science (EMFISIS) instrument (Kletzing et al., 2013), covering frequencies from ∼10 Hz to 12 kHz. Energetic electrons are measured by the Magnetic Electron Ion Spectrometer instrument (Blake et al., 2013), which provides distributions for electrons at ∼30 keV to ∼4 MeV. We use electron density inferred from the upper hybrid frequency detected by the High Frequency Receiver (HFR) of the EMFISIS instrument (Kurth et al., 2015). Solar wind and geomagnetic indices, including interplanetary magnetic fields (IMF), flow velocity, proton density, dynamic pressure, geomagnetic AE, AL, Sym-H, and Asym-H indices are obtained from the OMNI data set (Papitashvili & King, 2020) with a 1-min time resolution.

In this study, we adopted the published method of identifying substorm events (Chu et al., 2015). The substorm onset time was identified using the mid-latitude positive bay (MPB) index (Chu et al., 2015; McPherron & Chu, 2016, 2017, 2018; McPherron et al., 2018), which detects the amplitude of the field-aligned currents in the substorm current wedge using magnetic perturbations at midlatitudes. The substorm onset was marked at the time when the MPB index started to increase, and further refined using raw magnetometer perturbations. Compared to auroral electrojet indices, the MPB index detects global substorms and is insensitive to pseudo-breakups and localized currents. The MPB onset has been quantitatively validated against the auroral onset observed by the IMAGE EUV instrument, showing an average timing difference of only 1.9 min (Chu et al., 2015).

We applied the method over the entire Van Allen Probes era from January 2013 to July 2019 and identified 4,071 substorm events in total. In this substorm events list, weak events (300–500 nT) account for 2,154 occurrences, moderate events (500–1,000 nT) account for 1,566 occurrences, and 351 events exceed 1,000 nT and are classified as intense.

We identify hiss waves based on the following criteria: (a) ellipticity greater than 0.7, (b) frequency between 20 Hz and the lower of either 4 kHz or the electron gyrofrequency, (c) occurrence within the plasmasphere or plumes. We use electron cyclotron harmonic (ECH) wave power, from the HFR measurements, in the frequency range between the electron gyrofrequency and 50 kHz, to determine whether the spacecraft is located inside or outside high-density plasmasphere or plume regions. Intervals with an average ECH wave power exceeding 3.5×10^{-13} $(V/m)^2/Hz$ are classified as being outside the plasmasphere or plume, while the rest of the intervals are classified as inside these regions. Although ECH waves have their own spatial distribution (Meredith et al., 2009; Zhou et al., 2023), in this study, they are used only as a density-based indicator to determine whether the spacecraft is located inside or outside the plasmasphere or plumes. Therefore, the spatial distribution of ECH wave amplitudes will not noticeably bias the hiss distributions. Exo-hiss waves (e.g., Gao et al., 2018; Zhu et al., 2015), which occur outside the plasmasphere, are intentionally excluded and therefore not analyzed in this work. We also require waves to be righ-hand polarized, which well removes EMIC waves and magnetosonic

waves. These wave and plasmasphere/plume selection methods have been validated through several previous studies (Chu et al., 2024; Huang et al., 2023; Shen et al., 2019). Hiss wave amplitude at each time slice is then calculated as $B_w = \sqrt{\int_{20\ \mathrm{Hz}}^{\min(4\ \mathrm{kHz}, f_{ce})} I_B df}$, where I_B is wave magnetic spectral density and df is the wave frequency bin size.

In this study, we analyze hiss wave power over a frequency range of 20 Hz–4 kHz (or up to the local electron cyclotron frequency), a band that includes both regular hiss (hundreds of Hz–several kHz) and low-frequency hiss (<∼200 Hz). Although previous work has shown that regular and low-frequency hiss can exhibit different features and drivers (e.g., Malaspina et al., 2017), our objective here is to characterize the overall spatial and temporal evolution of plasmaspheric hiss during substorms. An investigation of how each of the two frequency components evolves during substorms is left for future studies.

An example event is presented in Figure S1 in Supporting Information S1, where hiss waves exhibit a clear intensification following substorm onset. This temporal evolution highlights the close correlation between substorm activity and hiss waves. However, their global evolution during substorms cannot be easily determined from a single case study alone, due to the coupling between temporal and spatial variations.

3. Statistical Results

To evaluate global hiss wave evolution during substorms, we performed a superposed epoch analysis of hiss waves measured by the dual Van Allen Probes during the identified 4,071 substorm events.

3.1. Solar Wind and Geomagnetic Conditions During Selected Substorms

Figure 1 shows the superposed epoch analysis results of solar wind and geomagnetic conditions during the selected substorm events. Epoch time zero is defined as the substorm onset. A key feature observed prior to substorm onset (zero epoch time) is the reduction of the southward IMF B_z component, which is a critical condition for triggering substorms. Within half an hour of the peak southward IMF, substorm activity intensifies, as indicated by a sharp rise in the AE index, which reflects enhanced auroral electrojet currents. This feature is characteristic of substorms, which involve the sudden release of energy stored in the magnetotail, leading to enhanced auroral activity and electrojet currents. As the substorm evolves toward the recovery phase, IMF B_z returns to near-zero values, while the solar wind flow speed remains relatively steady throughout the event.

The Sym-H index, representing the ring current intensity, exhibits a gradual decrease instead of a sharp drop during the substorms, suggesting that these substorms are not necessarily always associated with geomagnetic storms. In contrast, the Asym-H index increases sharply after substorm onset, indicating enhanced asymmetry in the geomagnetic field, likely driven by intensified nightside currents (Iyemori & Rao, 1996). This asymmetry is typical during substorms, as the associated disturbances are often localized within specific regions of the magnetosphere or ionosphere. The MPB index shows a sharp increase right after the substorm onset, as expected. We note that, in this study, the MPB index is used solely for precise onset detection, whereas the AE index is used to classify substorm strength.

3.2. Hiss Wave Evolution During Substorms

Figure 2 presents the superposed epoch analysis result of hiss wave amplitude and 60 keV electron flux evolution across different phases of substorms. Each time slice from T1 through T5 (from left to right columns) indicates: the root-mean-squared (RMS) wave amplitudes, the average 60 keV electron flux, and the number of samples in each half-hour time interval, with the middle time point shown as dots in the top panel. Previous studies suggested that 10–100 keV electrons with anisotropic pitch angle distributions are critical for local whistler mode wave growth (Ni et al., 2014). In this study, we use 60 keV as a representative energy for these electrons. The electron flux used here is the omnidirectional flux and averaged over each bin. The top panel shows the superposed AE index for all selected substorm events. We select five time slices to show the global evolution of hiss waves and 60 keV electron fluxes during different phases of substorms.

Before substorm onset (T1 and T2), the peak hiss wave activity, with amplitudes of ∼20 pT, occurs in the postnoon-to-dusk sector at T1, and shifts toward the near-noon sector at T2, as the superposed AE index increases from ∼200 to ∼250 nT. Immediately following substorm onset (T3), hiss waves begin to intensify, with a

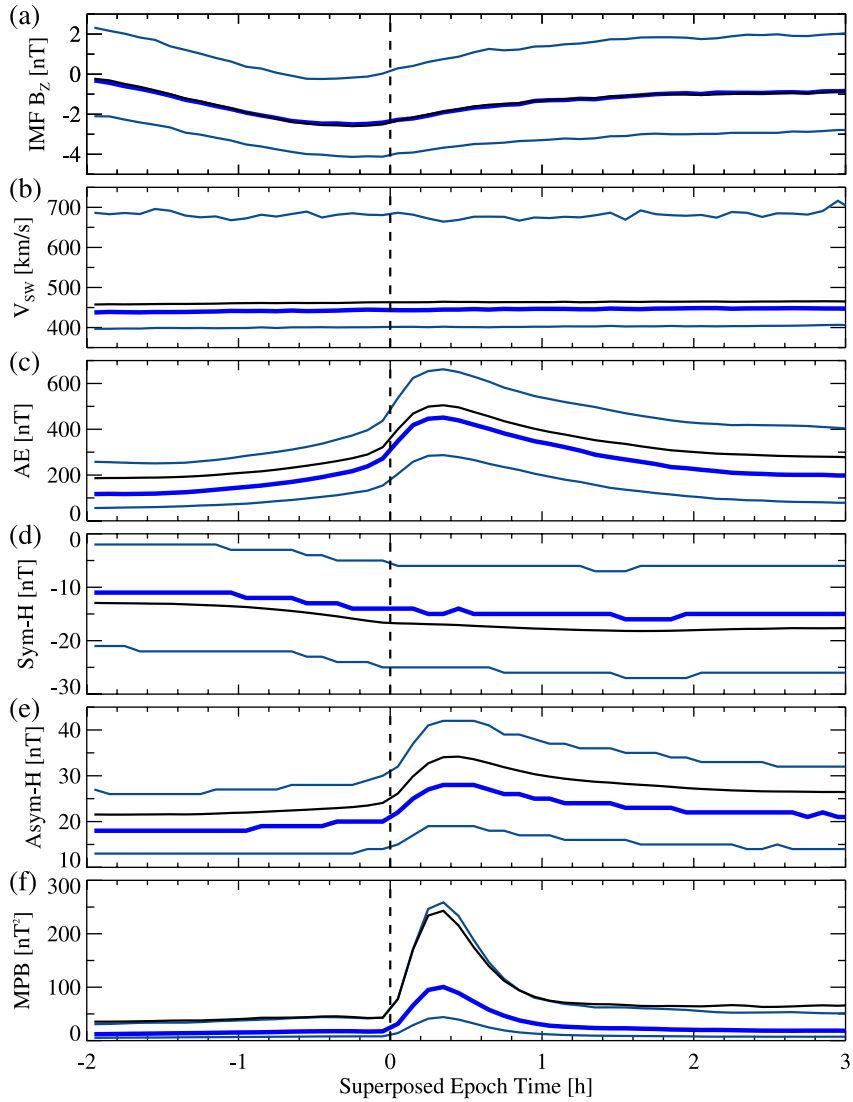

Figure 1. Superposed epoch analysis results of solar wind and geomagnetic parameters during selected 4,071 substorm events. (a) Interplanetary magnetic fields B_z component, (b) solar wind flow speed, (c) AE index, (d) Sym-H index, (e) Asym-H index, and (f) mid-latitude positive bay index. The blue and light blue lines represent the median and the lower/upper quartiles, respectively, and the black lines indicate the mean values. Zero epoch time is defined as the onset of each substorm event (vertical dashed line).

pronounced enhancement centered around ~06 MLT and L from 2 to 5. As time progresses (T4 and T5), the hiss wave enhancements exhibit a systematic movement toward later MLTs.

More interestingly, as the substorm progresses and the enhanced hiss wave enhancement region moves toward later MLTs, the electron flux exhibits a similar pattern to hiss waves at $L > 4$. The electron flux (at $L > 4$) initially presents a low level at T1 and T2, and increases shortly after the substorm onset (T3) over 06–12 MLT. Then the enhanced electron flux patch at $L > 4$ drifts toward later MLTs at T4 and T5.

To further examine the relationship between hiss wave amplitude and 60 keV electron flux, we calculate the average hiss wave amplitudes and 60 keV electron flux at $L > 4$ within four MLT sectors: 0–6, 6–12, 12–18, and 18–24 MLT, and plot their evolution as a function of superposed epoch time, spanning from 2 hr before to 3.5 hr after substorm onset in Figure 3. Results reveal that, from 0 to 18 MLT, hiss wave amplitude and 60 keV electron flux begin to increase coincident within our 30-min epoch resolution following substorm onset. In the 0–6 MLT sector, both hiss wave amplitude and 60 keV electron flux reach the peak within 0.5 hr after onset, while in later

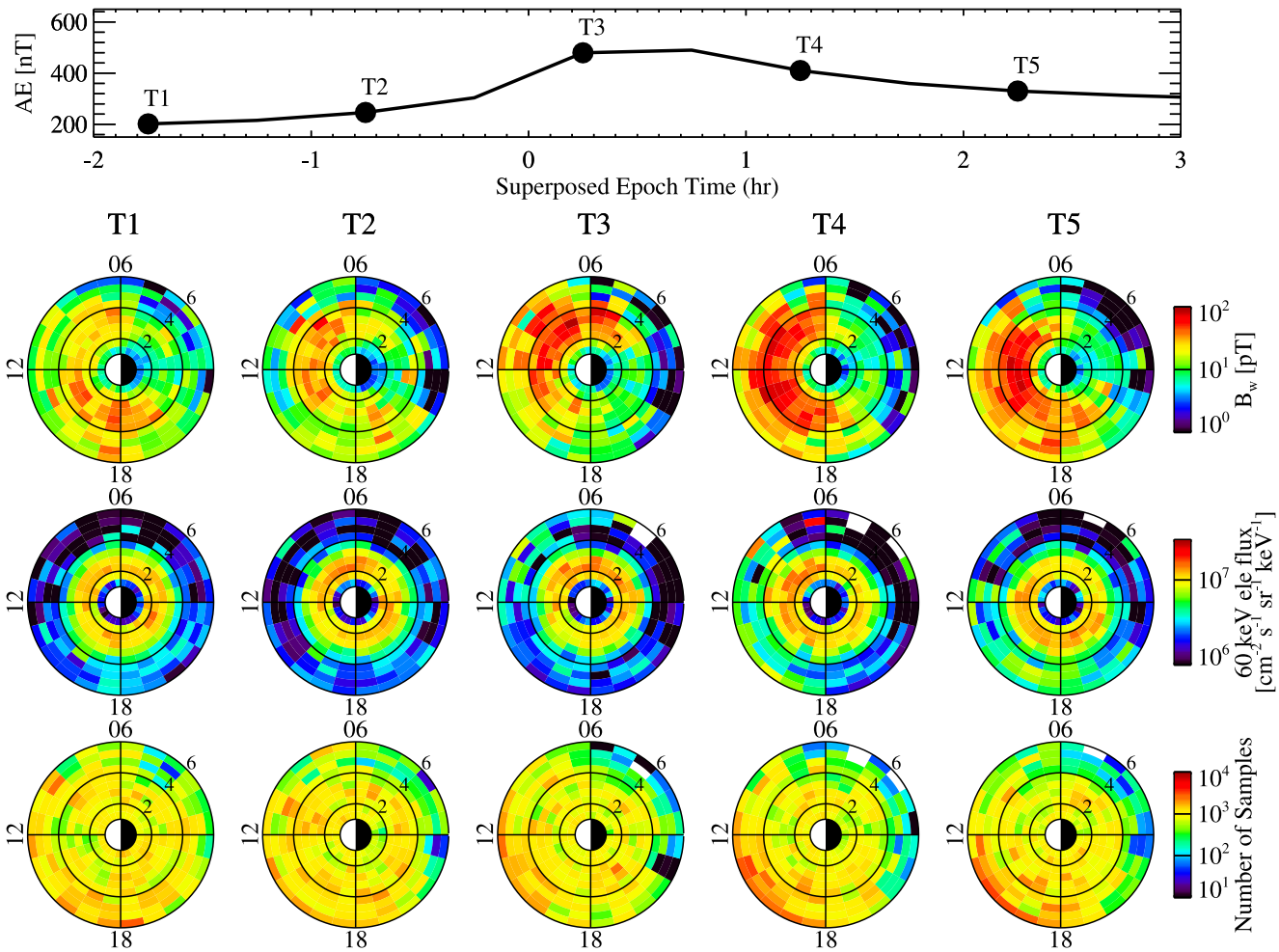

Figure 2. Superposed epoch analysis of global hiss wave amplitude and electron flux evolution during 4,071 substorms from 2013 to 2019, based on dual Van Allen Probes measurements. The top row presents the superposed AE index, with five times selected to evaluate wave and particle dynamics. The subsequent rows display the root-mean-squared hiss wave amplitude distribution, electron flux at 60 keV, and the number of samples in the L-magnetic local time map. Each column corresponds to one of the five times shown in the top row.

MLT sectors, their peak values occur progressively later. This feature validates the close relation between hiss waves and tens of keV electron fluxes within the plasmasphere or plumes at large L shells ($L > 4$) during substorms.

Lastly, we categorize substorm events based on the maximum AE index during each substorm as weak (300–500 nT), moderate (500–1,000 nT), and intense (>1,000 nT) substorms to examine the dependence of global hiss waves (L = 1–6, MLT = 0–24) on substorm intensity, as shown in Figure 4. Note that since epoch time zero is not the peak AE value, the peak superposed AE may therefore not show large values (Figure 4a). As expected, hiss waves show consistent features that their wave amplitude increases after substorm onset during weak, moderate and intense substorms. But during intense substorms, hiss wave amplitudes reach high values within 0.5 hr after substorm onset compared to those observed during less intense substorms, which may take up to 1.5 hr (Figure 4b). Moreover, the hiss wave amplitude enhancements during intense substorms last longer than weaker substorms. Weak substorms show a modest increase from ∼15 to ∼20 pT, whereas intense substorms show a comparable absolute increase but start from higher initial amplitudes and reach larger peak values overall.

To analyze how the hiss wave enhancement location evolves during substorms, we calculate the characteristic MLT (calculated as $\frac{\iint \mathrm{MLT} \times B_w \, dL \, d\mathrm{MLT}}{\iint B_w \, dL \, d\mathrm{MLT}}$) and the characteristic L-shell location (calculated as $\frac{\iint L \times B_w \, dL \, d\mathrm{MLT}}{\iint B_w \, dL \, d\mathrm{MLT}}$) of hiss waves (Figures 4c–4e) over 0–24 MLT and 1–6 L-shells. The sampling distributions as a function of L and MLT

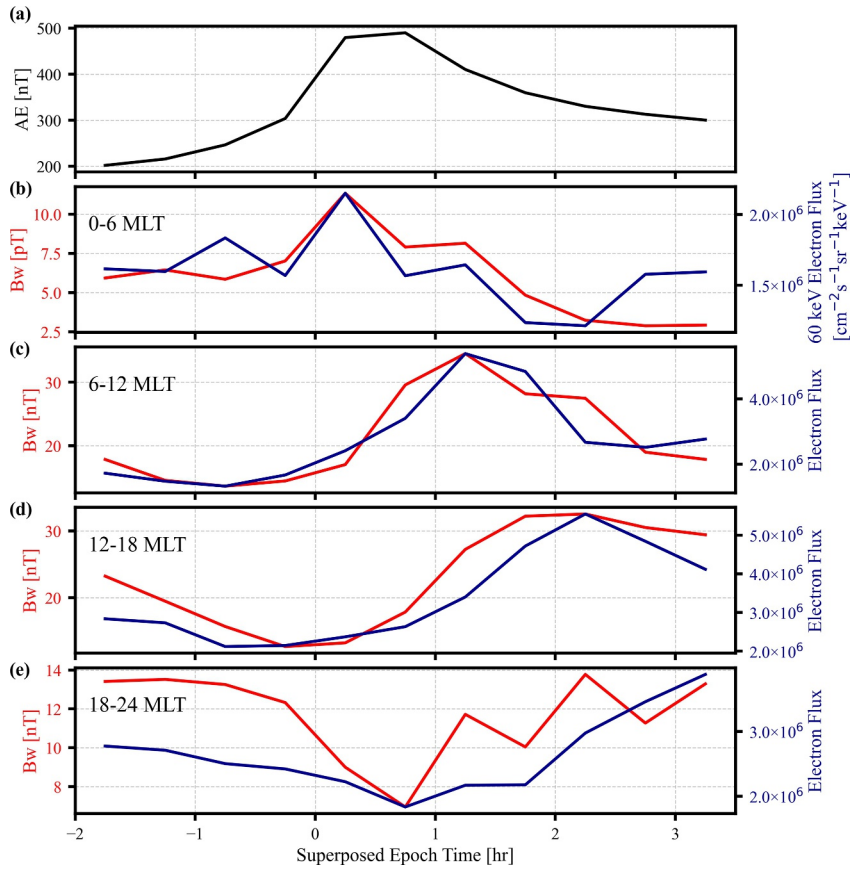

Figure 3. Superposed epoch analysis result of hiss wave amplitudes and 60 keV electron fluxes at $L > 4$ at four different magnetic local time (MLT) ranges. (a) Geomagnetic AE index. (b–e) Superposed epoch analysis result of root-mean-squared hiss wave amplitude and averaged 60 keV electron flux at L-shells from 4 to 6 over 0–6, 6–12, 12–18, and 18–24 hr MLT, respectively.

for weak, moderate, and intense substorms are shown in the Figure S1 in Supporting Information S1. The characteristic MLT distribution of plasmaspheric hiss exhibits a clear dependence on substorm intensity. For weak, moderate, and intense substorms, hiss wave activity consistently first intensifies in the morning sector and subsequently shifts toward the afternoon sector, indicating that this MLT evolution is a general feature rather than one confined to intense events. In contrast, intense substorms exhibit higher wave intensities and a faster initial progression toward the dayside compared with weaker substorm activity.

To quantify this temporal evolution, we compute the MLT progression rate $d\text{MLT}/dt$ (Figure 4d) as the finite difference of the characteristic MLT between consecutive epoch times divided by the 1-hr universal time spacing between epochs. Thus, $d\text{MLT}/dt$ is expressed in units of MLT hours per UT hour. Negative values correspond to a westward shift toward earlier MLTs, consistent with hiss intensification beginning on the morning side around substorm onset. Half an hour later, the MLT progression rate turns positive with values around ∼1–3 hr of MLT per hr of UT (slightly faster for more intense substorms). Around 2–3 hr after the substorm onset, the hiss waves, for all three levels of substorm intensities, begin to stabilize near 13 MLT (Figure 4c). At that time, the level of AE values returns to pre-substorm values. The characteristic L-shell location of hiss waves also exhibits a clear dependence on substorm intensity. During more intense substorms, hiss wave activity extends to higher L-shells within 30 min after substorm onset and to lower L-shells after 30 min, eventually reaching regions closer to Earth.

4. Summary and Discussion

The present study reveals hiss wave evolution on a global scale across various phases of substorms using the satellite data from the entire Van Allen Probes era. The superposed epoch analysis results indicate that, shortly after substorm onset, hiss waves typically intensify in the morning sector of the magnetosphere. As time

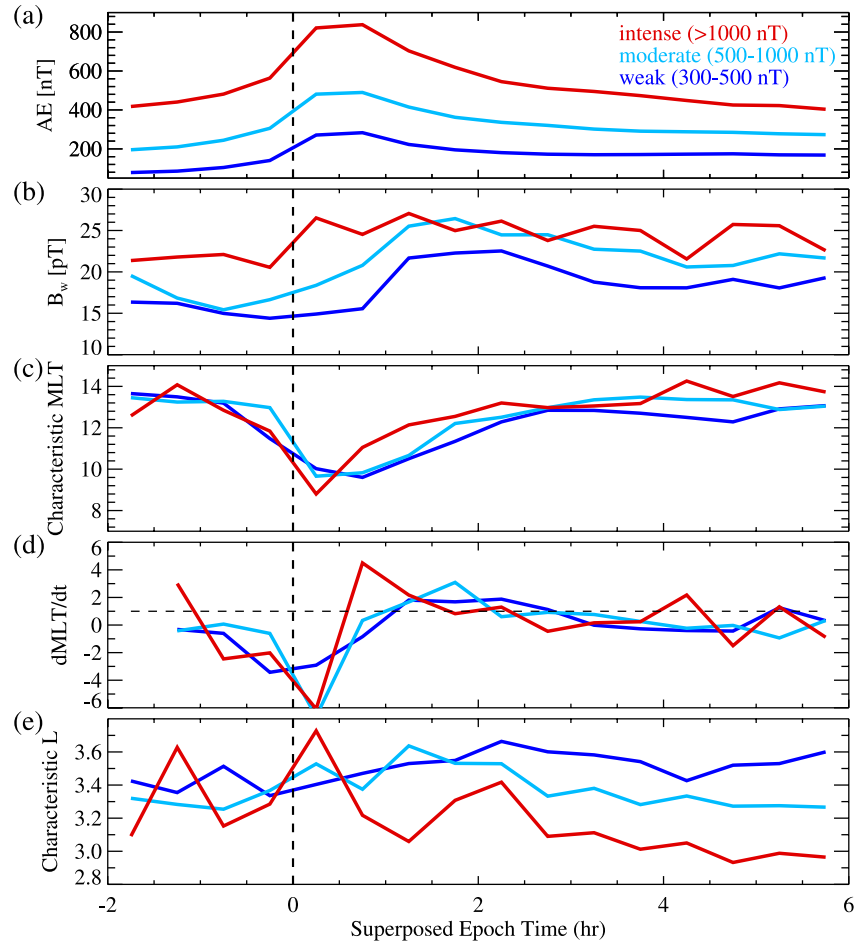

Figure 4. Superposed epoch analysis result of hiss wave evolution during three groups of substorms categorized by substorm intensity (the maximum AE index). (a) AE index, (b) root-mean-squared hiss wave amplitude, (c) characteristic magnetic local time (MLT), (d) MLT progression rate (*d*MLT/*dt*), where positive values indicate eastward movement (as viewed from the north), and (e) characteristic L-shell.

progresses, the wave activity moves toward later magnetic local times (MLTs) at a rate of approximately 1–3 hr MLT per hr UT, eventually stabilizing around 13 MLT.

Hiss wave dynamics are closely related to energetic electrons with ~60 keV. The intensification of hiss waves coincides with increased 60 keV electron flux, particularly at L-shells greater than 4, suggesting a strong relationship between wave intensity and substorm-injected electrons. It could be due to local hiss wave generations associated with the a portion of energetic electrons penetrating into the plasmasphere or plumes (He et al., 2019, 2020) at large L-shells or chorus waves intensification outside the plasmasphere, which then propagate into the plasmasphere (Bortnik et al., 2008, 2009; Bortnik, Chen, Li, Thorne, & Horne, 2011; Li et al., 2015). However, this statistical study focuses exclusively on hiss wave properties and does not analyze the characteristics of chorus waves in the plasma trough region. As a result, we are unable to draw definitive conclusions regarding the source of the observed hiss waves. A combined analysis of both chorus and hiss wave properties outside and inside the plasmasphere, along with local wave growth rate calculations, would be needed in the future to more quantitatively assess the origin of hiss waves during substorms.

Substorm intensity has a substantial impact on the evolution of hiss waves. During more intense substorms, hiss waves reach higher peak amplitudes more quickly, extending to lower L-shells, and progress more quickly toward the afternoon sector. A faster MLT progression of the hiss enhancement region may result from stronger plasmaspheric erosion driven by enhanced convection during intense substorms. These intense waves are expected to drive more efficient electron scattering, resulting in stronger electron precipitation and a more pronounced

depletion of the outer radiation belts. In contrast, weak substorms (300 < AE < 500 nT) produce weaker hiss wave activity, with limited spatial expansion and a slower MLT progression rate. Weaker substorms tend to confine hiss waves to higher L-shells, resulting in a more limited impact on electron flux and milder electron precipitation. Moreover, weaker substorms begin to subside earlier and show a faster decay trend within the 3.5-hr post-onset window.

In summary, our study provides a comprehensive statistical analysis of hiss wave evolution across various phases of substorm events, revealing a clear dependence on substorm intensity and highlighting the dynamic coupling between wave activity and energetic electron flux in the Earth's magnetosphere. These results also suggest the crucial role of hiss waves in mediating radiation belt dynamics, particularly in response to substorm activity. By evaluating temporal and spatial evolution of hiss waves during different phases of substorms, this study advances our understanding of inner magnetospheric processes and provides valuable insights for future modeling and forecasting of radiation belt electron dynamics.

Conflict of Interest

The authors declare no conflicts of interest relevant to this study.

Data Availability Statement

Data from the Van Allen Probes is publicly available at NASA's Space Physics Data Facility (SPDF): https://spdf.gsfc.nasa.gov/pub/data/. The solar wind and geomagnetic parameters are obtained from the OMNI data set (Papitashvili & King, 2020). We use SPEDAS in IDL to process data files (Angelopoulos et al., 2019). The substorm list used in this study is shared through figshare (Shen et al., 2025).

Acknowledgments
XS, WL, and QM would like to acknowledge the NASA Grants 80NSSC25K7686, 80NSSC24K0266, 80NSSC24K0239, 80NSSC21K1312, 80NSSC21K1385, 80NSSC20K0704, and 80NSSC24K0572, and NSF Grants AGS-2225445, AGS-2247774, AGS-2402179, and AGS-1847818. NM would like to acknowledge funding from the Natural Environment Research Council Grants NE/X000389/1 and NE/R016038/1. XC would like to thank Grants 80NSSC20K0196, 80NSSC22K1023, 80NSSC20K1325, 80NSSC23K0096, 80NSSC18K1227, 80NSSC24K1112, NSF Grant AGS-2247255, and AFOSR YIP FA9550-23-1-0359.

References

Agapitov, O., Mourenas, D., Artemyev, A., Claudepierre, S. G., Hospodarsky, G., & Bonnell, J. W. (2020). Lifetimes of relativistic electrons as determined from plasmaspheric hiss scattering rates statistics: Effects of ω_{pe}/Ω_{ce} and wave frequency dependence on geomagnetic activity. *Geophysical Research Letters*, *47*(13), e2020GL088052. https://doi.org/10.1029/2020GL088052

Angelopoulos, V., Cruce, P., Drozdov, A., Grimes, E. W., Hatzigeorgiu, N., King, D. A., et al. (2019). The Space Physics Environment Data Analysis System (SPEDAS). *Space Science Reviews*, *215*(1), 9. https://doi.org/10.1007/s11214-018-0576-4

Blake, J. B., Carranza, P. A., Claudepierre, S. G., Clemmons, J. H., Crain, W. R., Dotan, Y., et al. (2013). The magnetic electron ion spectrometer (MagEIS) instruments aboard the Radiation Belt Storm Probes (RBSP) spacecraft. *Space Science Reviews*, *179*(1–4), 383–421. https://doi.org/10.1007/s11214-013-9991-8

Bortnik, J., Chen, L., Li, W., Thorne, R. M., & Horne, R. B. (2011). Modeling the evolution of chorus waves into plasmaspheric hiss. *Journal of Geophysical Research*, *116*(A8), A08221. https://doi.org/10.1029/2011JA016499

Bortnik, J., Chen, L., Li, W., Thorne, R. M., Meredith, N. P., & Horne, R. B. (2011). Modeling the wave power distribution and characteristics of plasmaspheric hiss. *Journal of Geophysical Research*, *116*(A12), A12209. https://doi.org/10.1029/2011JA016862

Bortnik, J., Li, W., Thorne, R. M., Angelopoulos, V., Cully, C., Bonnell, J., et al. (2009). An observation linking the origin of plasmaspheric hiss to discrete chorus emissions. *Science*, *324*(5928), 775–778. https://doi.org/10.1126/science.1171273

Bortnik, J., Thorne, R. M., & Meredith, N. P. (2008). The unexpected origin of plasmaspheric hiss from discrete chorus emissions. *Nature*, *452*(7183), 62–66. https://doi.org/10.1038/nature06741

Breneman, A. W., Halford, A., Millan, R., McCarthy, M., Fennell, J., Sample, J., et al. (2015). Global-scale coherence modulation of radiation-belt electron loss from plasmaspheric hiss. *Nature*, *523*(7559), 193–195. https://doi.org/10.1038/nature14515

Chen, L., Li, W., Bortnik, J., & Thorne, R. M. (2012). Amplification of whistler-mode hiss inside the plasmasphere: Hiss growth. *Geophysical Research Letters*, *39*(8), L08111. https://doi.org/10.1029/2012GL051488

Chu, X., Bortnik, J., Shen, X.-C., Ma, Q., Li, W., Ma, D., et al. (2024). Imbalanced regressive neural network model for whistler-mode hiss waves: Spatial and temporal evolution. *Journal of Geophysical Research: Space Physics*, *129*(8), e2024JA032761. https://doi.org/10.1029/2024JA032761

Chu, X., McPherron, R. L., Hsu, T.-S., & Angelopoulos, V. (2015). Solar cycle dependence of substorm occurrence and duration: Implications for onset. *Journal of Geophysical Research: Space Physics*, *120*(4), 2808–2818. https://doi.org/10.1002/2015JA021104

Draganov, A. B., Inan, U. S., Sonwalkar, V. S., & Bell, T. F. (1992). Magnetospherically reflected whistlers as a source of plasmaspheric hiss. *Geophysical Research Letters*, *19*(3), 233–236. https://doi.org/10.1029/91GL03167

Gao, Z., Su, Z., Xiao, F., Zheng, H., Wang, Y., Wang, S., et al. (2018). Exohiss wave enhancement following substorm electron injection in the dayside magnetosphere. *Earth and Planetary Physics*, *2*(5), 359–370. https://doi.org/10.26464/epp2018033

Hayakawa, M., & Sazhin, S. S. (1992). Mid-latitude and plasmaspheric hiss: A review. *Planetary and Space Science*, *40*(10), 1325–1338. https://doi.org/10.1016/0032-0633(92)90089-7

He, Z., Chen, L., Liu, X., Zhu, H., Liu, S., Gao, Z., & Cao, Y. (2019). Local generation of high-frequency plasmaspheric hiss observed by Van Allen probes. *Geophysical Research Letters*, *46*(3), 1141–1148. https://doi.org/10.1029/2018GL081578

He, Z., Yu, J., Chen, L., Xia, Z., Wang, W., Li, K., & Cui, J. (2020). Statistical study on locally generated high-frequency plasmaspheric hiss and its effect on suprathermal electrons: Van Allen probes observation and quasi-linear simulation. *Journal of Geophysical Research: Space Physics*, *125*(10), e2020JA028526. https://doi.org/10.1029/2020JA028526

Huang, S., Li, W., Ma, Q., Shen, X.-C., Capannolo, L., Hanzelka, M., et al. (2023). Deep learning model of hiss waves in the plasmasphere and plumes and their effects on radiation belt electrons. *Frontiers in Astronomy and Space Sciences*, *10*, 1231578. https://doi.org/10.3389/fspas.2023.1231578

Iyemori, T., & Rao, D. R. K. (1996). Decay of the Dst field of geomagnetic disturbance after substorm onset and its implication to storm-substorm relation. *Annales Geophysicae*, *14*(6), 608–618. https://doi.org/10.1007/s00585-996-0608-3

Kim, K.-C., Shprits, Y., & Wang, D. (2020). Quantifying the effect of plasmaspheric hiss on the electron loss from the slot region. *Journal of Geophysical Research: Space Physics*, *125*(5), e2019JA027555. https://doi.org/10.1029/2019JA027555

Kletzing, C. A., Kurth, W. S., Acuna, M., MacDowall, R. J., Torbert, R. B., Averkamp, T., et al. (2013). The electric and magnetic field instrument suite and integrated science (EMFISIS) on RBSP. *Space Science Reviews*, *179*(1–4), 127–181. https://doi.org/10.1007/s11214-013-9993-6

Kurth, W. S., De Pascuale, S., Faden, J. B., Kletzing, C. A., Hospodarsky, G. B., Thaller, S., & Wygant, J. R. (2015). Electron densities inferred from plasma wave spectra obtained by the waves instrument on Van Allen probes: Van Allen probes electron densities. *Journal of Geophysical Research: Space Physics*, *120*(2), 904–914. https://doi.org/10.1002/2014JA020857

Li, W., Chen, L., Bortnik, J., Thorne, R. M., Angelopoulos, V., Kletzing, C. A., et al. (2015). First evidence for chorus at a large geocentric distance as a source of plasmaspheric hiss: Coordinated THEMIS and Van Allen probes observation: Origin of plasmaspheric hiss. *Geophysical Research Letters*, *42*(2), 241–248. https://doi.org/10.1002/2014GL062832

Li, W., Ni, B., Thorne, R. M., Bortnik, J., Nishimura, Y., Green, J. C., et al. (2014). Quantifying hiss-driven energetic electron precipitation: A detailed conjunction event analysis. *Geophysical Research Letters*, *41*(4), 1085–1092. https://doi.org/10.1002/2013GL059132

Li, W., Shen, X.-C., Ma, Q., Capannolo, L., Shi, R., Redmon, R. J., et al. (2019). Quantification of energetic electron precipitation driven by plume whistler mode waves, plasmaspheric hiss, and exohiss. *Geophysical Research Letters*, *46*(7), 3615–3624. https://doi.org/10.1029/2019GL082095

Li, W., Thorne, R. M., Bortnik, J., Reeves, G. D., Kletzing, C. A., Kurth, W. S., et al. (2013). An unusual enhancement of low-frequency plasmaspheric hiss in the outer plasmasphere associated with substorm-injected electrons. *Geophysical Research Letters*, *40*(15), 3798–3803. https://doi.org/10.1002/grl.50787

Liu, N., Su, Z., Gao, Z., Zheng, H., Wang, Y., Wang, S., et al. (2020). Comprehensive observations of substorm-enhanced plasmaspheric hiss generation, propagation, and dissipation. *Geophysical Research Letters*, *47*(2), e2019GL086040. https://doi.org/10.1029/2019GL086040

Ma, Q., Li, W., Thorne, R. M., Bortnik, J., Reeves, G. D., Kletzing, C. A., et al. (2016). Characteristic energy range of electron scattering due to plasmaspheric hiss. *Journal of Geophysical Research: Space Physics*, *121*(12), 11737–11749. https://doi.org/10.1002/2016JA023311

Ma, Q., Li, W., Zhang, X.-J., Bortnik, J., Shen, X.-C., Connor, H. K., et al. (2021). Global survey of electron precipitation due to hiss waves in the Earth's plasmasphere and plumes. *Journal of Geophysical Research: Space Physics*, *126*(8), e2021JA029644. https://doi.org/10.1029/2021JA029644

Malaspina, D. M., Jaynes, A. N., Hospodarsky, G., Bortnik, J., Ergun, R. E., & Wygant, J. (2017). Statistical properties of low-frequency plasmaspheric hiss. *Journal of Geophysical Research: Space Physics*, *122*(8), 8340–8352. https://doi.org/10.1002/2017JA024328

Mauk, B. H., Fox, N. J., Kanekal, S. G., Kessel, R. L., Sibeck, D. G., & Ukhorskiy, A. (2013). Science objectives and rationale for the radiation belt storm probes mission. *Space Science Reviews*, *179*(1–4), 3–27. https://doi.org/10.1007/s11214-012-9908-y

McPherron, R. L., Anderson, B. J., & Chu, X. (2018). Relation of field-aligned currents measured by the network of iridium® spacecraft to solar wind and substorms. *Geophysical Research Letters*, *45*(5), 2151–2158. https://doi.org/10.1002/2017GL076741

McPherron, R. L., & Chu, X. (2016). Relation of the auroral substorm to the substorm current wedge. *Geoscience Letters*, *3*(1), 12. https://doi.org/10.1186/s40562-016-0044-5

McPherron, R. L., & Chu, X. (2017). The mid-latitude positive Bay and the MPB index of substorm activity. *Space Science Reviews*, *206*(1), 91–122. https://doi.org/10.1007/s11214-016-0316-6

McPherron, R. L., & Chu, X. (2018). The midlatitude positive Bay index and the statistics of substorm occurrence. *Journal of Geophysical Research: Space Physics*, *123*(4), 2831–2850. https://doi.org/10.1002/2017JA024766

Meredith, N. P., Bortnik, J., Horne, R. B., Li, W., & Shen, X.-C. (2021). Statistical investigation of the frequency dependence of the chorus source mechanism of plasmaspheric hiss. *Geophysical Research Letters*, *48*(6), e2021GL092725. https://doi.org/10.1029/2021GL092725

Meredith, N. P., Horne, R. B., Bortnik, J., Thorne, R. M., Chen, L., Li, W., & Sicard-Piet, A. (2013). Global statistical evidence for chorus as the embryonic source of plasmaspheric hiss. *Geophysical Research Letters*, *40*(12), 2891–2896. https://doi.org/10.1002/grl.50593

Meredith, N. P., Horne, R. B., Clilverd, M. A., Horsfall, D., Thorne, R. M., & Anderson, R. R. (2006). Origins of plasmaspheric hiss. *Journal of Geophysical Research*, *111*(A9), A09217. https://doi.org/10.1029/2006JA011707

Meredith, N. P., Horne, R. B., Glauert, S. A., & Anderson, R. R. (2007). Slot region electron loss timescales due to plasmaspheric hiss and lightning-generated whistlers. *Journal of Geophysical Research*, *112*(A8), A08214. https://doi.org/10.1029/2007JA012413

Meredith, N. P., Horne, R. B., Kersten, T., Li, W., Bortnik, J., Sicard, A., & Yearby, K. H. (2018). Global model of plasmaspheric hiss from multiple satellite observations. *Journal of Geophysical Research: Space Physics*, *123*(6), 4526–4541. https://doi.org/10.1029/2018JA025226

Meredith, N. P., Horne, R. B., Thorne, R. M., & Anderson, R. R. (2009). Survey of upper band chorus and ECH waves: Implications for the diffuse aurora: Survey of upper band chorus and ECH waves. *Journal of Geophysical Research*, *114*(A7), A07218. https://doi.org/10.1029/2009JA014230

Meredith, N. P., Horne, R. B., Thorne, R. M., Summers, D., & Anderson, R. R. (2004). Substorm dependence of plasmaspheric hiss. *Journal of Geophysical Research*, *109*(A6), A06209. https://doi.org/10.1029/2004JA010387

Millan, R. M., & Thorne, R. M. (2007). Review of radiation belt relativistic electron losses. *Journal of Atmospheric and Solar-Terrestrial Physics*, *69*(3), 362–377. https://doi.org/10.1016/j.jastp.2006.06.019

Ni, B., Bortnik, J., Thorne, R. M., Ma, Q., & Chen, L. (2013). Resonant scattering and resultant pitch angle evolution of relativistic electrons by plasmaspheric hiss. *Journal of Geophysical Research: Space Physics*, *118*(12), 7740–7751. https://doi.org/10.1002/2013JA019260

Ni, B., Li, W., Thorne, R. M., Bortnik, J., Green, J. C., Kletzing, C. A., et al. (2014). A novel technique to construct the global distribution of whistler mode chorus wave intensity using low-altitude POES electron data: A novel technique for global wave model. *Journal of Geophysical Research: Space Physics*, *119*(7), 5685–5699. https://doi.org/10.1002/2014JA019935

Papitashvili, N. E., & King, J. H. (2020). OMNI 1-min Data [Dataset]. *NASA Space Physics Data Facility*. https://doi.org/10.48322/45bb-8792

Shen, X.-C., Li, W., Capannolo, L., Ma, Q., Qin, M., Artemyev, A. V., et al. (2023). Modulation of energetic electron precipitation driven by three types of whistler mode waves. *Geophysical Research Letters*, *50*(8), e2022GL101682. https://doi.org/10.1029/2022GL101682

Shen, X.-C., Li, W., Ma, Q., Agapitov, O., & Nishimura, Y. (2019). Statistical analysis of transverse size of lower band chorus waves using simultaneous multisatellite observations. *Geophysical Research Letters*, *46*(11), 5725–5734. https://doi.org/10.1029/2019GL083118

Shen, X.-C., Li, W., Ma, Q., Meredith, N., Chu, X., Qin, M., et al. (2025). Dataset for hiss wave evolution during substorms based on Van Allen probes observations [Dataset]. *figshare*. https://doi.org/10.6084/m9.figshare.30900212.v1

Sonwalkar, V. S., & Inan, U. S. (1988). Wave normal direction and spectral properties of whistler mode hiss observed on the DE 1 satellite. *Journal of Geophysical Research*, *93*(A7), 7493–7514. https://doi.org/10.1029/JA093iA07p07493

Spasojevic, M., Shprits, Y. Y., & Orlova, K. (2015). Global empirical models of plasmaspheric hiss using Van Allen probes. *Journal of Geophysical Research: Space Physics*, *120*(12), 10370–10383. https://doi.org/10.1002/2015JA021803

Thorne, R. M., Smith, E. J., Burton, R. K., & Holzer, R. E. (1973). Plasmaspheric hiss. *Journal of Geophysical Research*, *78*(10), 1581–1596. https://doi.org/10.1029/JA078i010p01581

Tsurutani, B. T., Park, S. A., Falkowski, B. J., Lakhina, G. S., Pickett, J. S., Bortnik, J., et al. (2018). Plasmaspheric hiss: Coherent and intense. *Journal of Geophysical Research: Space Physics*, *123*(12), 10009–10029. https://doi.org/10.1029/2018JA025975

Zhang, W., Ni, B., Huang, H., Summers, D., Fu, S., Xiang, Z., et al. (2019). Statistical properties of hiss in plasmaspheric plumes and associated scattering losses of radiation belt electrons. *Geophysical Research Letters*, *46*(11), 5670–5680. https://doi.org/10.1029/2018GL081863

Zhao, H., Ni, B., Li, X., Baker, D. N., Johnston, W. R., Zhang, W., et al. (2019). Plasmaspheric hiss waves generate a reversed energy spectrum of radiation belt electrons. *Nature Physics*, *15*(4), 367–372. https://doi.org/10.1038/s41567-018-0391-6

Zhou, Q., Li, J., Xiao, F., Zhang, S., Liu, S., Yang, C., et al. (2023). Global occurrence of higher-bands ECH waves in radiation belts based on a novel noise reduction algorithm (NORA). *Geophysical Research Letters*, *50*(6), e2022GL101889. https://doi.org/10.1029/2022GL101889

Zhu, H., Su, Z., Xiao, F., Zheng, H., Wang, Y., Shen, C., et al. (2015). Plasmatrough exohiss waves observed by Van Allen probes: Evidence for leakage from plasmasphere and resonant scattering of radiation belt electrons. *Geophysical Research Letters*, *42*(4), 1012–1019. https://doi.org/10.1002/2014GL062964